RESEARCH ARTICLE

Attenuation of hypersonic second-mode boundary-layer instability with an ultrasonically absorptive silicon-carbide foam

Carson L. Running[1] · Benjamin L. Bemis[1] · J. Luke Hill[1,2] · Matthew P. Borg[1,3] · Joel J. Redmond[1,4] · Karl Jantze[4] · Carlo Scalo[4]

Abstract

Unsteady surface pressure measurements have been carried out on a flat-plate test article in the Air Force Research Laboratory's Mach-6 Ludwieg Tube at a negative angle of attack using PCB pressure sensors. The acoustic waves of the second-mode boundary-layer instability mechanism were successfully measured as indicated by the fluctuating surface pressure spectra. The effectiveness of a novel porous material (Silicon-Carbide (SiC) foam) at absorbing these fluctuations was investigated by comparing porous-wall and impermeable-wall spectra. The impermeable-wall spectra indicate second-mode peaks in amplitude, which agree with companion computations, while the equivalent porous material showed no signs of the instability in the spectra therefore exhibiting a strong dampening ability. However, the porous-wall spectra demonstrate similar breakdown to turbulence to the impermeable material at higher length Reynolds numbers, which might be attributed to surface-roughness effects. Acoustic-absorption bench tests also indicated high levels of ultrasonic absorption for the SiC foam—the acoustic absorption coefficient was consistently higher than 0.90 for second-mode relevant frequencies. A band-limited amplitude integration of the experimental PCB spectra indicate lower amplitude growth in the porous material compared to the impermeable material; however, beyond a length Reynolds number of $\approx 4 \cdot 10^6$, the band-limited amplitude of the porous material approach a similar value to the impermeable one. Linear-stability (LST) computations confirmed the experimentally observed frequencies only when supported by base-flow calculations capturing the leading-edge shock, which entails sudden thickening of the boundary layer at the tip not captured by the Blasius solution. Computed N factors for the porous material were approximately 30% of the associated impermeable values where the material inserts were located, downstream of which, they approached the same value. This study indicates that SiC foam has a strong ability to absorb acoustic waves characteristic of the hypersonic second-mode boundary-layer instability mechanism, and is therefore a candidate material for passive boundary-layer control.

1 Introduction

The state of the boundary layer (i.e., laminar, transitional, or turbulent) on hypersonic vehicles has a significant effect on the heat transfer and shear-stress loads imparted on the surface. The thermal protection systems (TPS) to shield these considerable aerothermodynamic loads remain a dominant design consideration — a more massive TPS required imposes significant mass and efficiency penalties on the vehicle's performance (Anderson 2006). Reed et al. (1997) indicate that the surface heat flux on a realistic hypersonic flight vehicle experiencing a turbulent boundary layer would be approximately five times higher compared to a laminar one, which would approximately double the overall TPS weight. Similar results have been indicated elsewhere in the literature (Force 1992), and therefore emphasize the vital role that boundary-layer transition has on hypersonic flight.

The ability to control the state of the boundary layer has consequently become a considerable effort in the hypersonic research community. Active (e.g., plasma actuators (Yates et al. 2020), blowing/suction (Johnson et al. 2009), wall

✉ Carson L. Running
  crunning1@udayton.edu

[1] Department of Mechanical and Aerospace Engineering, University of Dayton, Dayton, OH 45469, USA

[2] Air Force Institute of Technology, WPAFB, Dayton, OH 45433, USA

[3] Air Force Research Laboratory, WPAFB, Dayton, OH 45433, USA

[4] HySonic Technologies, LLC, West Lafayette, IN 47906, USA

cooling/heating (van Driest and Boison 1957)) as well as passive (e.g., isolated/distributed roughness (Saikia and Brehm 2022), porous surfaces (Wagner et al. 2013), etc.) techniques have been studied resulting in various degrees of boundary-layer state manipulation (Kimmel 2003). Porous walls may be incorporated synergistically into existing TPS, making them an intriguing and potentially realizable control solution (Wagner et al. 2013).

There are various boundary-layer instability mechanisms that arise in the hypersonic flight regime, such as first mode, second mode, and crossflow, depending on flow conditions and vehicle geometry. The second-mode instability traditionally begins to dominate the boundary-layer transition process for two-dimensional (e.g., slender and/or symmetric geometries at small angles of attack) boundary layers for Mach numbers of approximately four and above (Mack 1984), and will be the focus of the current study. The second-mode instability manifests itself as propagating ultrasonic acoustic waves trapped between the vehicle surface and the relative sonic line (Mack 1984). Seminal experimental investigations conducted by Demetriades (1974), Kendall (1975), and Stetson (1983) established the existence and role of the second-mode instability. The study of this instability mechanism continues to this day and its history/evolution is well documented throughout the literature.

The fundamental working principle of incorporating porous materials (sometimes referred to as ultrasonically absorptive coatings (UAC)) as a boundary-layer flow-control technique is their ability to absorb acoustic waves. Porous walls absorb/subtract energy from modes that leave an unsteady pressure footprint at the surface and can therefore be geometrically designed/tuned to waves that are characteristic of the second mode, potentially leading to a reduction in unstable growth. Malmuth et al. (1998) first illustrated this phenomenon via Linear Stability Theory (LST), which was quickly supported experimentally under Mach-5 flow in the T-5 hypersonic wind tunnel at Caltech (Fedorov et al. 2001; Rasheed et al. 2002). These early works incorporated materials with regularly-spaced micro holes; however, the push to integrate the technology with TPS, which often has irregular porosity, led to studies of materials with irregular porous structures, such as: felt metal (Fedorov et al. 2003, 2006), nylon mesh (Lukashevich et al. 2018), and porous carbon–carbon (Wagner et al. 2013; Wartemann et al. 2015; Sousa et al. 2019). Direct numerical simulations (DNS) of transition delay were carried out for the first time in Sousa et al. (2019) by modeling carbon–carbon material through the usage of the time domain impedance boundary condition (Fung and Ju 2004; Scalo et al. 2015). This was the first instance in which the experimentally measured wall impedance has

been shown to delay turbulence in computational fluid dynamics (CFD) for hypersonic flows. The computational work herein will utilize this technique in order to support the experimental findings.

The current study builds upon these previous works, and introduces a new candidate random-porosity material—Silicon-Carbide (SiC) foam (Miller et al. 2022; Bemis et al. 2023), to attenuate the hypersonic second-mode boundary-layer instability. Although the integration of SiC foam into a TPS is outside the scope of the current investigation, the material does have a number of unique features and is customizable. Metallic foams, such as SiC, are traditionally used in heat exchangers, air oil separators, baffles, energy absorbers, CO_2 scrubbers, flame arrestors, filters, breather plugs, electrodes, electromagnetic interference shields, optics, and biomedical applications. The SiC foam used in this study is Duocel® Silicon-Carbide Foam from ERG Aerospace Corporation and is detailed in Sect. 2.2 below. It is a highly porous material comprised of a rigid skeletal structure. Figure 1 shows a magnified view of the SiC foam wall-normal surface topography used in the current study.

The current study investigates the absorptivity of the hypersonic second-mode boundary-layer instability via SiC foam on a flat-plate test article using PCB surface pressure sensors. The experimental facilities, test article, and flow conditions are provided in Sect. 2, followed by an outline of the data reduction methodology in Sect. 3. The supporting bench-test acoustic absorption model and computations are detailed in Sects. 4 and 5, respectively. The resulting data and discussion are given in Sect. 6.
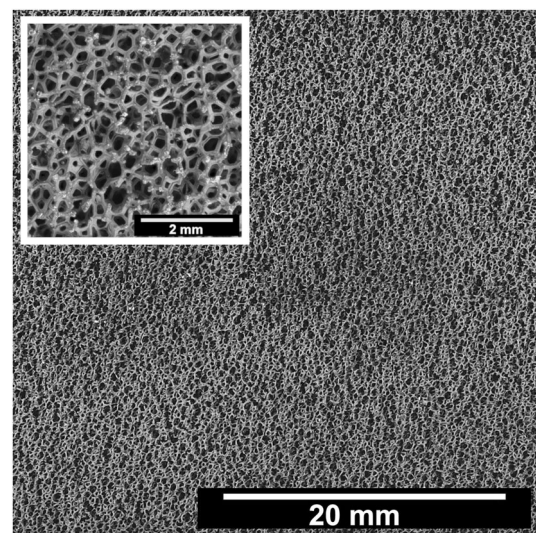

Fig. 1 Magnified view of the SiC foam wall-normal surface topography

2 Experimental setup

2.1 Wind tunnel

The wind-tunnel data presented herein were collected in the Air Force Research Laboratory's (AFRL) Mach-6 Ludwieg Tube (Kimmel et al. 2017). The tunnel has a 0.762-m-diameter, Mach-6 nozzle. Recent measurements of the flow have shown that the freestream Mach number is 6.1. A value of $M_\infty = 6.1$ is used throughout the current work (where the subscript ∞ represents a freestream condition upstream of any shock waves emanating from the test article). A custom plug-type fast valve in the contraction exit is used to start the tunnel. Root-mean-squared pitot pressure fluctuations are approximately 3% of the mean pitot pressure (Kimmel et al. 2017). Tests consist of two periods of steady flow, each of which is approximately 100 ms long. Data from the middle 50% (i.e., 50 ms) of each of the two periods were used in the analyses to follow.

The stagnation pressure p_0 of the flow is measured with a Kulite pressure sensor flush-mounted upstream of the nozzle contraction. The p_0 values used for each test condition are determined by calculating the mean value from the Kulite over the middle 50% of each period. The gas temperature T_0 prior to being processed by the initial expansion wave is set to 505 K. Using isentropic relations from the measured p_0 data, the mean T_0 was calculated. The mean values for the freestream unit Reynolds number Re_∞ can be calculated utilizing the Sutherland viscosity law (Sutherland 1893) for the fluid's freestream viscosity, μ_∞. A total of six initial test conditions were executed spanning the operating range of the facility. The same initial conditions were used for the porous and impermeable materials. These six conditions result in a total of twelve unique conditions due to the two periods of steady flow per test.

The test article was installed at a relatively small negative angle of attack to ensure that the surface sensors were on the compression side of the model and to obtain higher second-mode frequencies. Due to pre-first-period deflections of the test article, it was determined that the most accurate measurement of its angle of attack, α, relative to the incoming freestream came from high-speed schlieren visualization measurements of the leading-edge shock angle. The α was then calculated via inviscid oblique-shock relations, $\alpha = -1.1 \pm 1.0$, resulting in a post-shock Mach number of

Table 1 Experimental wind-tunnel flow conditions for data presented herein

Material	Condition	M_∞	p_0 (kPa)	T_0 (K)	Re_∞ ($\cdot\ 10^6$ /m)	$Re_{\infty,\mathrm{PS}}$ ($\cdot\ 10^6$ /m)
Impermeable	1	6.1	492	460	4.6	4.8
	2	6.1	609	489	5.1	5.4
	3	6.1	748	459	7.0	7.4
	4	6.1	932	489	7.8	8.3
	5	6.1	984	458	9.2	9.7
	6	6.1	1230	489	10.3	11.0
	7	6.1	1467	458	13.7	14.5
	8	6.1	1837	488	15.4	16.4
	9	6.1	1955	458	18.3	19.4
	10	6.1	2452	488	20.6	21.9
	11	6.1	2444	458	22.9	24.3
	12	6.1	3065	488	25.8	27.4
Porous	1	6.1	490	460	4.6	4.8
	2	6.1	609	489	5.1	5.4
	3	6.1	748	459	7.0	7.4
	4	6.1	932	489	7.8	8.3
	5	6.1	988	459	9.2	9.7
	6	6.1	1230	489	10.3	11.0
	7	6.1	1468	458	13.7	14.5
	8	6.1	1835	488	15.4	16.4
	9	6.1	1956	458	18.3	19.4
	10	6.1	2450	488	20.6	21.9
	11	6.1	2430	458	22.7	24.1
	12	6.1	3044	488	25.6	27.2

5.9 (see Sect. 3.2 below for more details on this α calculation process). Note, the conservatively large range of uncertainty in α is not indicative of facility-wide α uncertainty or test-to-test changes in angle of attack since nothing about the physical setup was changed; therefore, it is acceptable to make direct comparisons between data sets. Table 1 shows the mean flow properties relevant to data used throughout this work, including the post-shock unit Reynolds number, $Re_{\infty,PS}$. The largest observed percent difference in Re_∞ between the two materials for a given test condition was 0.9%, which is small. Uncertainty ranges for the reported freestream properties was not possible since the Mach-number uncertainty, driver-tube gas temperature stratification, and viscosity uncertainty were all unknown. Estimates of Mach-number uncertainty can be inferred from Kimmel et al. (2017) and Hsu et al. (2020); however, accurate assessments of the spatial-temporal uncertainty/variation have not been conducted.

2.2 Wind-tunnel test article

A flat plate with a nominally sharp leading edge was used in this work. Although cones are more commonly used to investigate the second-mode boundary-layer instability, a flat plate offers a more convenient test bed due to the complexities of manufacturing non-planar ultrasonically absorptive porous materials. See references (Fedorov et al. 2001; Maslov et al. 2001; Fedorov 2003; Fedorov et al. 2003; Roediger et al. 2008; Egorov et al. 2008; Heitmann et al. 2011; Kegerise and Rufer 2016) for previous works studying the hypersonic second-mode instability mechanism on flat-plate geometries. The test article was made from stainless steel. An initial 10° taper from the leading edge was used on the underside of the test article. Modifications were made to the test article before measurements could be made of the leading edge uniformity/sharpness. The test-article geometry is provided in Fig. 2 with relevant dimensions in units of millimeters. A cavity for the different material inserts was cut
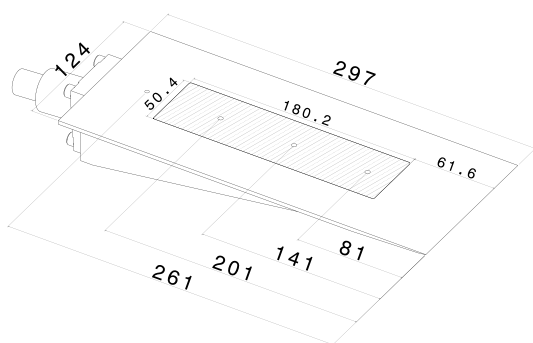
on the top surface. The material inserts were bolted into this cavity from the underside of the test article. Shims were used to align the inserts with the top surface of the test article. Small gaps on the order of 0.01 mm were observed in the corners of the two inserts. Edge effects from the leading-edge corners of the test article were approximated before the experiments by calculating the Mach angle for Mach-6.1 flow and tracking how it proceeds toward the centerline of the test article. The yaw angle is fixed by the tunnel sting, and the roll angle was measured as 0.0° with a digital angle indicator having an overall uncertainty of $\pm 0.2°$. The distance from the nozzle exit plane to the test article's leading edge was 114 mm. Figure 3 shows the instrumented test article installed in the wind-tunnel test section with the impermeable material insert.

The impermeable material used was standard polyether ether ketone (PEEK). The porous material was Duocel® Silicon-Carbide (SiC) Foam from ERG Aerospace Corporation. The relative density of the foam used was 8–15%. The relative density parameter is a percentage, or volume fraction, of the material within the foam's ligaments compared to the entire bulk volume that the structure takes up (i.e., the inverse of porosity). The pores per linear millimeter was 3.9 for the foam in this work. See Fig. 1 above for a magnified image of the SiC foam used in the current work.

The test article was instrumented with four flush-mounted 132B38/010PH pressure sensors from PCB Piezotronics. Three of the sensors were placed in the material inserts, while one was inserted downstream of the insert. The axial location, x, (measured from the leading edge of the test article) of sensors 1, 2, 3, and 4 was 81 mm, 141 mm, 201 mm, and 261 mm, respectively. The sensors were electronically
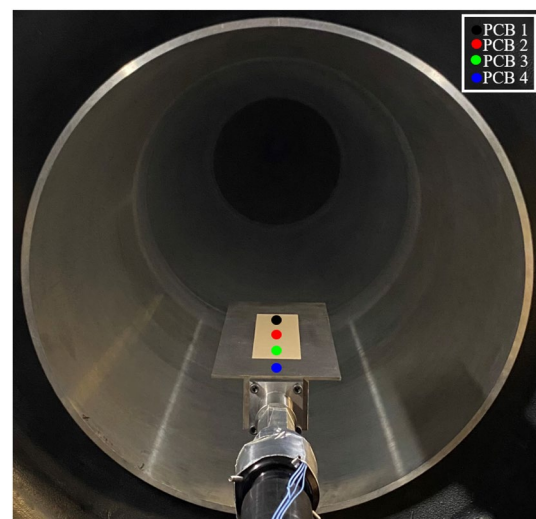

Fig. 2 Flat-plate test article (units in mm). Hashed lines indicate material insert location

Fig. 3 Flat-plate test article in the wind-tunnel test section (flow is out of the page). Black, red, green, and blue dots represent PCB sensors 1, 2, 3, and 4, respectively. Impermeable material insert

insulated with shrink wrap and nail polish was used as the adhesive per suggestions in Ort and Dosch (2019). The same four sensors were used (in the same locations) for the two materials.

High-speed schlieren visualization was used to image the leading-edge shock wave on the test article. A Newport 66,921 Arc Lamp with a power output of 600 W was used as the light source. A Photron Fastcam SA-Z-2100 K collected images at 20 kHz. A horizontal knife edge was used in order to be sensitive to wall-normal density gradients. See Oddo et al. (2021) for more details on the schlieren setup in the AFRL Mach-6 Ludwieg Tube.

3 Data reduction methodology

3.1 PCB pressure sensors

The AC-coupled PCB data were sampled at 5 MHz and conditioned via a 482C signal-conditioning box from PCB Piezotronics. The factory calibration constants were used to dimensionalize the data resulting in the fluctuating component of surface pressure, p'. Figure 4 shows a second-mode wave packet evolution through sensors 1–4 for a representative test with the impermeable material ($Re_\infty = 4.6 \cdot 10^6$ /m). The black, red, green, and blue lines represent sensors 1, 2, 3, and 4, respectively. The vertical axis for sensors 2–4 have each been vertically offset from each other by a value of 0.1 kPa in order to highlight the packet evolution.
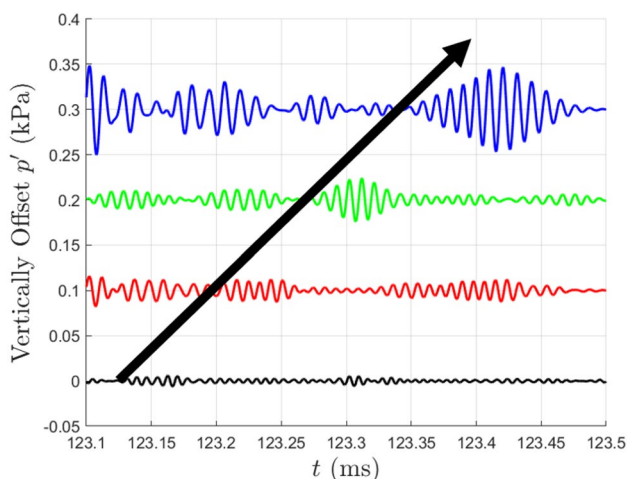

Fig. 4 Vertically offset p' time series at sensor locations 1–4 indicating the wave packet evolution. Black, red, green, and blue lines represent sensors 1, 2, 3, and 4, respectively. Impermeable material at $Re_\infty = 4.6 \cdot 10^6$ /m
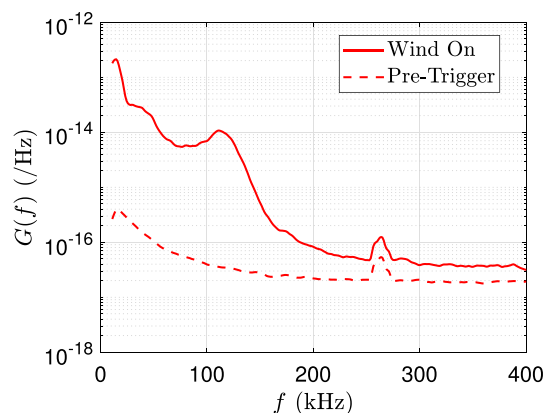

Fig. 5 $\frac{p'}{p_\infty}$ power spectra (semi-logarithmic vertical scaling) of sensor 2. Solid and dashed lines represent wind-on and wind-off data, respectively. Impermeable material at $Re_\infty = 4.6 \cdot 10^6$ /m

3.1.1 Power spectra

The power spectral density (PSD) of the $\frac{p'}{p_\infty}$ signal was calculated via the Welch method (Welch 1967). The analysis incorporated 2500-point segments with 50% overlap. Each segment was windowed with a Hamming window. The sampling rate divided by the window size yields the frequency resolution of the methodology (i.e., 2 kHz). The PSD is represented by $G(f)$, where f is the temporal frequency. The units of $G(f)$ are (/Hz). A ± 8 kHz moving average filter was used on the spectral data.

Noise was observed in many of the spectra, most notably around $f \approx 300 \pm 50$ kHz. The source of this noise is still undetermined. Figure 5 provides the sensor-2 spectra for the impermeable material at $Re_\infty = 4.6 \cdot 10^6$ /m. The solid and dashed lines represent the wind-on and wind-off (i.e., pre-trigger) spectra for that sensor, respectively.

The spectral data for these frequency bands of noise have been linearly interpolated over herein. This was done by finding the frequency ranges of spectral noise in the pre-trigger data for each sensor and linearly interpolating between the beginning and end frequencies of that data when present in the wind-on spectra.

The PCB-4 data have also been omitted herein out of an abundance of caution due to concerns of edge effects from the corners of the leading edge of the test article. Although the test-article design accounted for these via Mach-6.1 waves from the leading-edge corners, the spectral behavior from PCB-4 data indicated boundary-layer transitional trends inconsistent with the other sensors and computations.

3.2 High-speed schlieren

High-speed schlieren measurements were used to measure the angle of the shock wave associated with the leading edge of the test article. The background-subtracted schlieren images (i.e., those where the pre-run image was subtracted) were time-averaged over the middle 50% of each flow period for each test condition resulting in a single image for each of the twenty-four conditions shown in Table 1. The test article's angle of attack, α, relative to the incoming freestream was then calculated from the shock angle via the inviscid, two-dimensional, oblique-shock relations. This resulted in a value of $\alpha = -1.1° \pm 1.0°$ for all of the tests (Table 1). The uncertainty in α stems from the wavy nature of the leading-edge shock wave (which is partly a result of the spanwise integration effect and/or edge effect of the schlieren measurements on a flat plate), uncertainty in the freestream conditions, and uncertainty in the inviscid/two-dimensional assumptions used in the oblique-shock calculations. The absolute uncertainty stemming from the spanwise integration and model edge effects are difficult to isolate/quantify. The uncertainty of $\alpha = -1.1° \pm 1.0°$ is not representative of a test-to-test change in α. Figure 6 provides a representative instantaneous snapshot of the schlieren data collected, where the test-article's leading-edge shock wave, porous insert leading edge, and PCB sensors 1–3 are all visible and labeled. The angle between the leading-edge shock wave and the test-article's surface provided measurements of the leading-edge shock angle.

4 Absorption measurements via ultrasonic bench tests

4.1 Previous ultrasonic bench-test setups

The ultrasonic absorption data of the SiC foam porous material presented herein was collected using a pressure-controlled ultrasonic absorption bench test developed by HySonic Technologies inspired by previous work
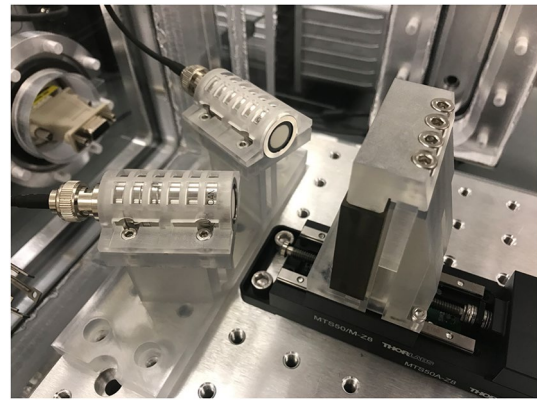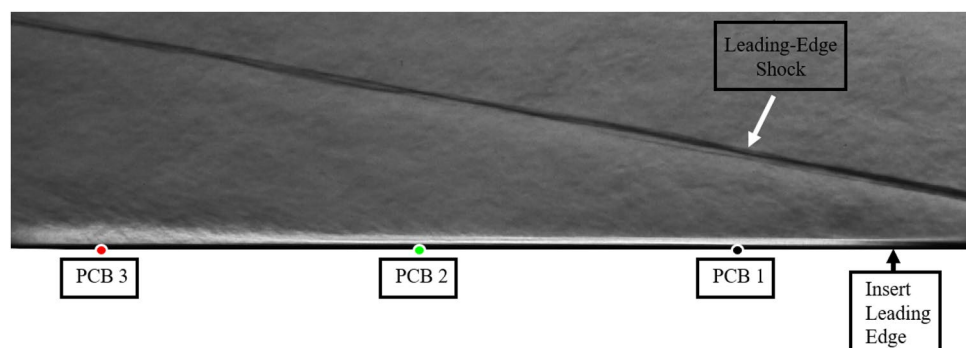

Fig. 7 Pressure-controlled ultrasonic absorption bench test

(Tsyryulnikov and Mironov 2004; Wagner et al. 2014). Bench-test measurements are used to inform the broadband complex impedance boundary condition used in the supporting computations (see Sect. 4.5).

Ultrasonic absorption testing carried out within the context of second-mode boundary-layer instability control was first performed by Tsyryulnikov and Mironov (2004), where the absorption of thin porous coatings was evaluated using two methods: (1) an acoustico-interferometric technique, detailed by Rosin (1972), which required a resonant tube (with 2 kPa minimum pressure), housing a piezoceramic ultrasonic transmitter, the material sample, and a capacitor microphone (limited to 52 kHz); (2) direct comparison between an ultrasonic pulse reflected off the porous sample to that of an impermeable reference material. The second method inspired the work by Wagner et al. (2014) and the present study.

4.2 Current ultrasonic bench-test setup

The bench-test setup in this work follows closely the one by Wagner et al. (2014). It is composed of a vacuum chamber, air-coupled ultrasonic probe pairs, and a data acquisition system that uses a waveform generator, amplifier, and oscilloscope to generate and receive high-frequency signals. The

Fig. 6 Annotated instantaneous schlieren snapshot (flow is right to left). Porous material at $Re_\infty = 18.3 \cdot 10^6$ /m

ultrasonic probes are fastened to a fixture mounted at an angled position on an optical bread board located within the vacuum chamber. The angled position allows the acoustic angle of incidence impinging upon the sample to be varied from 16.0° to 40.0° where 0.0° represents perpendicular (or direct) impingement. The ultrasonic probe fixture includes a translation stage used to place the porous sample at the distance from the probes that maximized reflection. Dry air (as opposed to pure nitrogen) is employed and the ultrasonic probes are driven up to 400 $V_{pk\text{-}pk}$ (as opposed to 160 $V_{pk\text{-}pk}$), which leads to acoustic absorption measurements at pressures lower than in Wagner et al. (2014), while still higher than those in the experimental wind tunnel tests.

The ultrasonic probes used herein were made by SONO-TEC GmbH, and were operated at frequencies of 75, 125, 200, and 300 kHz. Figure 7 shows the bench-test setup in the vacuum chamber with the 200-kHz probes.

4.3 Experimental measurement of the absorption coefficient

The ultrasonic bench test provides a direct measurement of the absorption coefficient, β,

$$\beta = 1 - |R^2|, \tag{1}$$

related to the reflection coefficient R given by

$$R = \frac{A_{porous}}{A_{ref}}, \tag{2}$$

where A_{porous} and A_{ref} are the amplitude in Volts, recorded by the oscilloscope, of the waves reflected off the porous and impermeable (i.e. reference) samples, respectively, with an error of ± 8 mV at a given pressure. For each oscilloscope measurement, there is a pressure measurement taken using an MKS Baratron capacitance manometer with an allowable tolerance of 0.12% of the pressure reading (i.e. $\pm$ 1.2 Pa at 1 kPa base pressure to $\pm$ 24 Pa at 20 kPa base pressure). The reflection amplitudes were measured with a National Instruments Oscilloscope (PXIe-5172) at a sampling rate of 20 MHz with a 1 MΩ impedance. This allows for 266 voltage measurements per acoustic cycle at 75 kHz down to 40 voltage measurements per acoustic cycle at 500 kHz.

Table 2 Ultrasonic probe aperture dimensions and low pressure limit

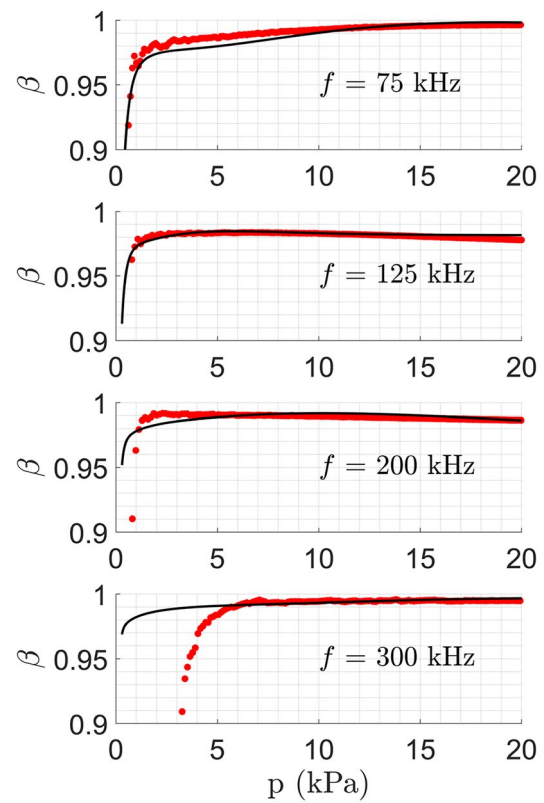| f (kHz)	ø (mm)	A (mm²)	p_{min} (Pa)
75	30.0	706.9	614.3
125	19.0	283.5	781.7
200	11.0	95.0	810.4
300	7.0	38.5	3264.1

Fig. 8 Measurements of ultrasonic absorption β of the SiC foam (red dots) obtained at four discrete frequencies compared against fitted JCA model (black line) with coefficients in Table 3

Data is collected for chamber pressures in the 0.2–20 kPa range, with approximately 50 Pa increments, using a 100-μm diameter flow orifice in line with a computer-controlled solenoid valve fed by a compressed air tank regulated at 690 kPa. This allowed for choked flow at the orifice providing near constant pressure changes to occur between each data point.

Lower-frequency probes produce measureable signals for base pressures lower than the higher-frequency probes due to the inherently more favorable air-coupling at lower frequencies and their larger aperture diameter (see Table 2).

The absorption data for the SiC foam was collected at an acoustic angle of 40.0° and is shown with red dots in Fig. 8. This data is compared against the Johnson-Champoux-Allard (JCA) model detailed below.

4.4 Formulation of JCA model

The Johnson-Champoux-Allard Model offers a theoretical prediction for the complex broadband impedance $Z(\omega)$ of porous-material samples with specified properties (discussed below).

The impedance $Z(\omega)$ is defined as

$$\hat{p}(\omega) = -Z(\omega)\hat{v}, \tag{3}$$

where $\hat{p}$ and $\hat{v}$ are the Fourier transforms of the pressure and velocity fluctuations normal to the surface of the porous material exposed to the flow. Here a wall-normal velocity fluctuation is taken as positive if directed away from the porous wall and into the flow. The complex impedance is often normalized by the base impedance $Z_0 = \rho_0 a_0$ (real value), defined as the product of the base speed of sound a_0 and density ρ_0. For $Z(\omega) = Z_0$, the porous material behaves as a perfect acoustic black hole, absorbing all of the acoustic energy directed at it under a normal angle of incidence. The base impedance is herein calculated based on a temperature of $T_0 = 296$ K, speed of sound $a_0 = \sqrt{\gamma R T_0}$, and density $\rho_0 = p_0/RT_0$, which varies as a function of the pressure measured in the bench-test vacuum chamber.

The complex impedance $Z(\omega)$ is directly related to the reflection coefficient in Eq. 2, and hence β, via

$$R = \left| \frac{Z \cos\theta - Z_0}{Z \cos\theta + Z_0} \right|, \tag{4}$$

where θ is the impingement angle of the incident wave ($\theta = 0$ indicates normal incidence). For the current bench-test apparatus θ is set to 40.0°.

Finally, the JCA model reads:

$$Z = \frac{Z_\infty}{\tanh(jk_a d)}, \tag{5}$$

where Z_∞ and k_a are given by:

$$Z_\infty = \frac{Z_0}{\phi}\sqrt{\frac{\tilde{\tau}_J}{\tilde{T}_{CA}}} \quad \text{and} \quad k_a = \frac{\omega}{a_0}\sqrt{\tilde{\tau}_J \tilde{T}_{CA}}, \tag{6}$$

and d is the sample thickness while ϕ is the porosity. The model contains a viscous, $\tilde{\tau}_J$, and a thermal, $\tilde{T}_{CA}$, term defined as,

$$\tilde{\tau}_J = \kappa\left(1 - j\frac{\sigma\phi}{\kappa\omega\rho_0}\sqrt{1 + j\mu\omega\rho_0\left[\frac{2\kappa}{\sigma\phi k_v}\right]^2}\right), \tag{7}$$

and

$$\tilde{T}_{CA} = \gamma - \left(\frac{\gamma - 1}{1 - j\frac{\sigma\phi}{\kappa\omega\rho_0 Pr}\sqrt{1 + j\mu\omega\rho_0 Pr\left[\frac{2\kappa}{\sigma\phi k_t}\right]^2}}\right). \tag{8}$$

The viscous and thermal terms, $\tilde{\tau}_J$ and $\tilde{T}_{CA}$, are dimensionless and are functions of the flow resistivity, σ, the porosity, ϕ, the tortuosity, κ, which is restricted to values greater than 1, the characteristic viscous boundary-layer length, k_v,

Table 3 JCA model coefficients for the SiC foam

f (kHz)	d (mm)	ϕ (%)	σ (Pa· s/m²)	κ
75	5.85	86.2	9957.5	1.65
125	5.85	86.2	9816.6	1.64
200	5.85	86.2	9323.6	1.59
300	5.85	86.2	9041.9	1.57

the characteristic thermal boundary length, k_t among other parameters, such as viscosity, μ, ambient density, ρ_0, and the angular frequency, ω. As detailed by Allard and Champoux (1992), the characteristic viscous boundary-layer length k_v, and the characteristic thermal boundary length, k_t, are given by,

$$k_v = 0.64\sqrt{\frac{8\kappa\mu}{\sigma\phi}} \qquad , k_t = 1.64\sqrt{\frac{8\kappa\mu}{\sigma\phi}}. \tag{9}$$

4.5 Fitting of JCA model against bench-test data

The experimental bench-test data is shown in Fig. 8 (red dots) alongside the JCA model (black line) with coefficients (Table 3) derived via least-square fitting. The SiC foam used in the current study exhibits values of acoustic absorption exceeding 0.90 across the entire dataset.

The JCA model is adopted by assuming air with a gas constant of $R = 287.0$ J/kg K, ratio of specific heats of $\gamma = 1.4$, and Prandtl number of $Pr = 0.7$. The fluid dynamic viscosity, μ, was calculated via the Sutherland viscosity law using a viscosity reference value of $\mu_0 = 1.7894 \cdot 10^{-5}$ Pa · s, a reference temperature of $T_0 = 273.15$ K, and $S_\mu = 110.56$ (see Sutherland (1893)). An acoustic angle of incidence of $\theta = 40.0°$, matching the geometrical configuration of the bench-test experiments, was used throughout. The angular frequency is given by $\omega = 2\pi f$. Finally, values of sample depth (or thickness), d, are fixed by the material coupon tested.

To determine the rest of the unknown coefficients, the JCA model is incorporated into an optimization routine that finds the best combination of: porosity, ϕ; flow resistivity, σ; and tortuosity, κ. A single value of porosity is used, while values of σ and κ are allowed to change as a linear function of frequency during the optimization process as suggested by Champoux and Allard (1991). The resulting fitted values are shown in Table 3 with decreasing values for flow resistivity, σ, and tortuosity, κ as the ultrasonic frequency increases. The porosity value is not treated as a linear function of frequency but remains a tunable parameter. Each tunable parameter is given a reasonable and restrictive range to ensure physical results. For

instance, tortuosity cannot be less than 1. The JCA model coefficients, specifically flow resistivity, σ, and tortuosity, κ, produced by the optimization routine detailed in Sect. 4.4 were compared against those published in Table 3 of Sousa et al. (2019), which used the flow resistivity values for the C/C measured by Wagner et al. (2014). This C/C material showed a flow resistivity near $\sigma \approx 13.3$ MPa $\cdot$ s/m^2 and a tortuosity, κ, of 8.0. The silicon-carbide material in this present study is significantly more porous, less dense, and was found via the optimization routine to have a flow resistivity three orders of magnitude less than the C/C material tested by Wagner et al. (2014). The frequency-dependent flow resistivity and tortuosity for the silicon carbide material is given in Table 3.

The discrepancies between the fitted JCA model and the experimental absorption are largest at low pressures and/or high frequencies. The difficulty of measuring ultrasonic acoustic characteristics in a low-density medium is well known and discussed by Tsyryulnikov and Mironov (2004). Contributing to this problem is the size of the ultrasonic probe apertures, which limits the amount of acoustic power that can be transmitted into the low-density medium. The 200 kHz and 300 kHz probes have smaller aperture diameters compared to the lower frequency probes as seen in Table 2. Wagner et al. (2014) also noted a discrepancy in the theoretical model used at low pressures, however, in the opposite direction as what is observed here. This may be due to the higher starting pressure of the results provided by Wagner et al. (2014).

While the JCA model has not been developed for the ultrasonic regime, it is still used in this and previous work as a convenient low-order modeling framework to interpret the ultrasonic absorption measurements and subsequently provide impedance boundary conditions for the companion linear stability calculations. The JCA model does not account for rarefied-gas effects at low pressures. This limitation, combined with inherent impedance-mismatch issues at low pressures, decreases the accuracy of both predictive models and the measurements for $p < 1$ kPa.

In spite of these uncertainties, the extrapolated impedance values in the pressure range relevant to the wind tunnel tests
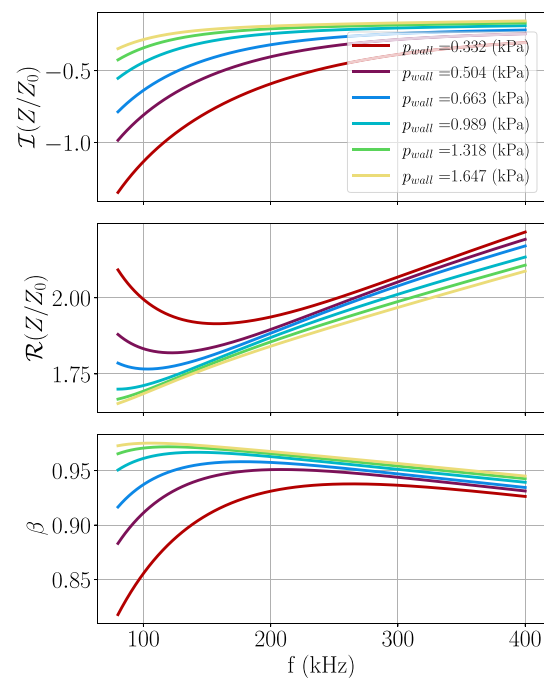

Fig. 9 Wall impedance boundary-condition model used by LST from bench-test JCA model (Table 3). See Table 4 for legend information. The impedance and absorption values shown here are extrapolated at these pressures due to limitations of the bench-test experiment discussed in Sect. 4.5

(0.3–1.6 kPa) exhibit the expected monotonic trend with static wall pressure values (see Fig. 9).

5 Computational modeling

To complement the experimental wind-tunnel measurements, a Linear Stability Theory (LST) study was conducted on selected base flows for test conditions 1, 3, 5, 7, 9, and 11 in Table 1 (see Table 4 for the full LST conditions).

5.1 Navier–Stokes Solver (H3AMR)

Initial LST analyses showed that using Blasius' solution to generate the baseflow for the stability analyses leads to

Table 4 Flow conditions used in the computational modeling

Re_∞ ($\cdot\ 10^6$ /m)	M_∞	p_∞ (Pa)	T_∞ (K)	u_∞ (m/s)	ρ_∞ (kg/m^3)	α (°)	Legend Color
4.6	6.1	281	55	903	0.01799	− 1.1	
7.0	6.1	428	54	902	0.02742	− 1.1	
9.2	6.1	563	54	901	0.03615	− 1.1	
13.7	6.1	839	54	901	0.05039	− 1.1	
18.3	6.1	1118	54	901	0.07181	− 1.1	
22.9	6.1	1399	54	901	0.08978	− 1.1	

significant over-prediction of the most amplified second-mode frequencies. This result was also observed in Roediger et al. (2008). There are a number of hypotheses for why this occurs, including the flow not being able to recover from memory affects initiated by the leading edge.

For this reason, a new spectral-difference (SD) solver H3AMR (**H**ySonic, **H**ybrid, **H**igh-Order, **A**daptive **M**esh **R**efinement), developed by HySonic Technologies was used to more accurately capture the viscous interactions between the shock and the sharp leading edge, hence improving the laminar base flow predictions used in the stability analyses. H3AMR is a compressible Navier–Stokes solver that relies on an Nth-order polynomial reconstruction of the solution within each element. The solution point that the polynomial reconstruction lives on is on the Legendre-Gauss (i.e., the zeros of the (N+1)th order Legendre polynomial). This approach follows the method outlined by Kopriva and Kolias (1996) and allows for a spectral convergence rate of the solution as the order increases. Flow discontinuities (i.e., shock waves) are handled by Riemann Solvers to add background dissipation between elements and through the use of Local Artificial Diffusion (Premasuthan et al. 2014; Haga and Kawai 2019) to add dissipation for shock waves within elements. H3AMR adopts a third-order Runge–Kutta time advancement.

The base flow for each condition reported was obtained on a two-dimensional mesh of 70,000 elements. A third-order local discretization was used within each element yielding 16 degrees of freedom per element, resulting in a total of 1.12 million degrees of freedom. The first mesh spacing off the wall is 0.2 mm leading to at least 13 third-order elements within the boundary layer at PCB location 1 for the highest freestream Reynolds number listed in Table 4. This yields 52 degrees of freedom in the wall-normal direction.

The simulations were carried out for four flow-through times to allow a sufficient settling time of all viscous and wave processes, hence achieving a steady base flow. Grid convergence was conducted using the highest Reynolds number case in Table 4 (condition 6), being the one with the most stringent requirements. It was determined that grid convergence was obtained once the boundary-layer profiles no longer changed at the first PCB probe location. Once grid convergence was achieved for the highest freestream Reynolds number, it was assumed that the same mesh could be used on all of the lower freestream Reynolds numbers.

To validate the accuracy of the linear stability calculations supported by the base flow generated by H3AMR, unsteady simulations were also conducted, in which a small perturbation was added near the tip of the plate and then allowed to convectively develop. As the perturbation travels, the most unstable second-mode frequencies emerge allowing them to be measured using an FFT of the time-probed pressure taps at the wall. The results of this study are depicted later in Fig. 11b below, where the plus signs indicate second-mode frequencies observed in the CFD calculations and the solid lines depict the second-mode frequencies predicted by LST. Plot demarcations of similar color represent similar freestream Reynolds numbers (Table 4). Both show good agreement with one another.

The pulse was applied through the implementation of a single period of wall suction and blowing at a designated location similar that used in Sivasubramanian and Fasel (2014) and Sousa et al. (2019). Equation 10 was utilized, where $A_p = \frac{1}{2}u_e = 44.8$ m/s is the amplitude of the pulse set to 5% of the boundary-layer edge velocity, $x_c = 0.015$ m and $w_p = 0.0025$ m are the center and width of the pulse, respectively. Finally, $f_p = 200$ kHz is the temporal frequency of the pulse. Note that even though a single frequency for the pulse is defined, the pulse is still broadband due to its compact spatio-temporal support.

$$v_p(x, t) = \begin{cases} A_p \cos^3\left((x - x_c)\frac{\pi}{w_p}\right)\sin(2\pi f_p t), & t < \frac{1}{f_p} \\ 0.0 & t \geq \frac{1}{f_p} \end{cases},$$

$$x \in \left[x_c - \frac{w_p}{2}, x_c + \frac{w_p}{2}\right] \tag{10}$$

5.2 Linear Stability Theory (LST)

The stability analysis was conducted using an in-house two-dimensional compressible linear stability solver developed for wall-bounded flows. The following sections describe the problem formulation and the global numerics scheme implemented in the solver.

5.2.1 Problem formulation

The Navier–Stokes equations were linearized under the assumption that the baseflow varies slowly in the axial direction, x, and that the perturbations are two dimensional, with the perturbation shape given under the Ansatz in Eq. 11. In this formulation, $\tilde{f}$ is the vector of perturbations in the primitive variables (ρ, u, v, p) that are being solved for, $\hat{f}(y)$ is the vector of shape functions for the primitive variables, ω is the frequency of the perturbation and finally κ_r, and κ_i are the real and imaginary parts of the complex wavenumber of the perturbation, respectively. The linearized compressible Naiver-Stokes equations assumed that the fluid was an ideal, perfect gas for thermodynamic closure, and used Sutherland's Law to calculate the viscosity as a function of temperature only (Sutherland 1893).

$$\tilde{f} = \hat{f}(y)e^{\kappa_r x}e^{j(\kappa_i x - \omega t)} \tag{11}$$

In the results presented herein, LST was conducted spatially with a fixed frequency for each case, while marching down the test article from $x = [5, 30]$ mm with a step size of $\Delta x = 0.5$ mm. The frequencies were from $f = [80, 400]$ kHz with a frequency step size of 2 kHz.

5.2.2 Numerical formulation

A spectral Laguerre-Galerkin discretization was used to solve the linear-stability equations. In this formulation, the solution was assumed to take the form of a polynomial expansion of a sum of known orthogonal basis functions and unknown weighting coefficients, which are solved for.

The Laguerre functions were chosen as the set of orthogonal basis functions because they are defined in the positive half of $\mathbb{R}^1$ and approach 0 as x approaches infinity, matching the assumed shape of the wall-normal perturbations in a hypersonic boundary layer. The first basis function is lifted, allowing the implementation of non-homogeneous Dirichlet boundary conditions at the wall. If a homogeneous Dirichlet boundary condition is desired, the first basis function is simply set to 0.

Because the Laguerre polynomials are defined from zero to infinity, as the order of the solver increases, the node locations move farther from the region of interest. To counteract this, a "false infinity" is imposed at $y = 5\delta$ where the last node is placed, with δ being the 99% boundary-layer thickness. A polynomial order of $N = 90$ was used in all of the calculations, as it sufficiently resolves the second-mode eigenvectors and eigenvalues of the solution. The reader is encouraged to reference the PhD Thesis by Sousa (2022) showing validation of this methodology for hypersonic flows over conical geometries under high cooling ratios.

5.2.3 Impedance boundary condition for LST

An impedance boundary condition was used to model the porous-wall cases. Traditional boundary-layer LST assumes that the fluctuating quantities $\hat{T}$, $\hat{u}$, $\hat{v}$ are zero at the wall (i.e., the Homogeneous Dirichlet boundary conditions). The implementation of the impedance boundary condition in the frequency domain is given by the simple relation in Eq. 12.

$$\hat{p} = Z(\omega)\hat{v} \tag{12}$$

While this is no longer a Dirichlet condition, the coupling between $\hat{p}$ and $\hat{v}$ at the wall simply results in another equation for the eigenvalue solver to solve.

Using the JCA model described in Sect. 4.4 with values given in Table 3, an analytic curve fit for the wall impedance $Z(\omega)$ as a function of wall pressure and frequency was defined using data from the acoustic absorption bench testing. Examples of these curve fits are shown for the wall

pressures associated with the six computational run conditions listed in Table 4 and are plotted in Fig. 9. Note that the pressures experienced along the surface of the flat plate test article wall are lower than what the bench-test data could directly record due to the limitations discussions in Sect. 4.5. As a result, the values of wall impedance and absorption in Fig. 9 are necessarily extrapolated. Results show minimal second-mode presence at these frequencies except at the highest Reynolds numbers. Because LST is conducted spatially for each frequency, one at a time, the curve fits were referenced to obtain a wall impedance for the specific frequency and pressure being computed.

6 Results and discussion
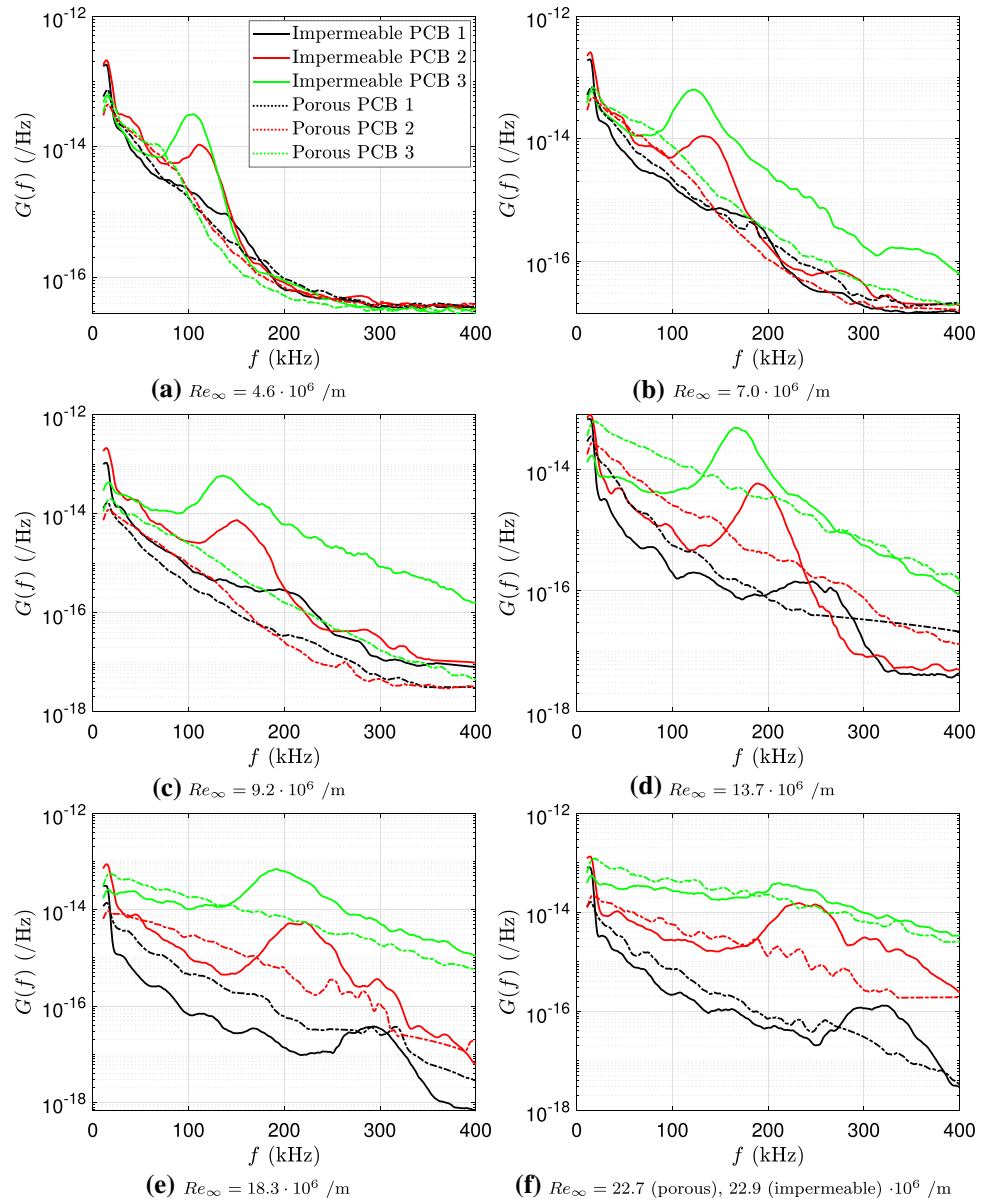
6.1 Power spectra

Figure 10 shows the experimental power spectra of $\frac{p'}{p_\infty}$ for test conditions 1, 3, 5, 7, 9, and 11 in Table 1. The solid and dot-dashed lines represent impermeable and porous data, respectively. The black, red, and green lines represent sensors 1, 2, and 3, respectively. The data are presented on a semi-logarithmic plot. The spectra are shown for $0 < f < 400$ kHz.

The impermeable spectra for relatively low Re_∞ (e.g., Fig. 10a) show clear amplitude peaks associated with the second-mode instability. The peaks increase in amplitude with increasing sensor location (i.e., increasing length Reynolds number, Re_x) indicative of the instability's growth. The frequency associated with the second-mode amplitude peaks decrease with sensor location due to the thickening of the boundary layer. These two trends continue for the impermeable data throughout all of the conditions, as expected.

Starting with the lower Re_∞ tests (e.g., Fig. 10a) again, the porous spectra indicate similar low-frequency ($f < 80$ kHz) content compared to their associated impermeable spectra, but decrease in relative amplitude in the second-mode relevant frequency range $80 < f < 350$ kHz. The lack of a spectral peak within this frequency range indicates that there is no apparent second-mode instability content or growth for the porous insert. This supports the bench-test results, which indicated that the foam has a strong ability to absorb acoustic waves characteristic of the second-mode instability.

The bicoherence of each signal was also calculated; however, there were no strong nonlinear interactions for any of the tests/materials. Likewise, harmonics are not observed in any of the spectra. Previous works investigating the second-mode instability mechanism on planar geometries have observed the same result (Stetson et al. 1991; Heitmann et al. 2011; Kegerise and Rufer 2016).

Fig. 10 Power spectra of $\frac{p'}{p_\infty}$ (semi-logarithmic vertical scaling). Solid and dot-dashed lines represent impermeable and porous walls, respectively. Black, red, and green lines represent sensors 1, 2, and 3, respectively

(a) $Re_\infty = 4.6 \cdot 10^6$ /m

(b) $Re_\infty = 7.0 \cdot 10^6$ /m

(c) $Re_\infty = 9.2 \cdot 10^6$ /m

(d) $Re_\infty = 13.7 \cdot 10^6$ /m

(e) $Re_\infty = 18.3 \cdot 10^6$ /m

(f) $Re_\infty = 22.7$ (porous), 22.9 (impermeable) $\cdot 10^6$ /m

The current study is focused on attenuation of the second-mode boundary-layer instability; however, it is still worth commenting on what the data might suggest regarding the physical transition location, while acknowledging that this is outside the scope of this work and data set. This physical boundary-layer transition location is often inferred from spectral broadening in boundary layers dominated by the second-mode instability (Stetson and Kimmel 1993); however, a number of previous studies on planar geometries have observed that the second mode may not be the driving mechanism responsible for breakdown to turbulence (Stetson et al. 1991; Wendt et al. 1993; Heitmann et al. 2011; Kegerise and Rufer 2016). All of these studies observed

considerable low-frequency ($f < 25$ kHz) content, which is consistent with the impermeable and porous spectra in Fig. 10. The spectra in Stetson et al. (1991) suggest that the second-mode instability actually persist through the main transition process, further indicating that it was not responsible for breakdown to turbulence. It is hypothesized that a similar phenomenon is present in the current data, while acknowledging that the inherent low-frequency (i.e., $f < 11$ kHz) resonance limit of the PCB sensors may have an effect on the low-frequency spectral amplitudes. This hypothesis is supported in Fig. 10b with the observation that the impermeable sensor-3 spectrum indicates a broad-band amplitude rise before a broadening of the second-mode

peak. It is also supported by the lack of harmonics observed in the bicoherence analysis of the data, which is consistent with other planar works (Stetson et al. 1991; Heitmann et al. 2011; Kegerise and Rufer 2016). Lastly, it is supported by the relatively low computed second-mode N factors detailed below. Therefore, the effect of a porous material on the boundary-layer transition location is left as an open question, which could be answered more thoroughly with the use of a global measurement technique (e.g., infrared thermography) and/or a conical test article exhibiting second-mode dominated transition. Future studies investigating this should also consider the possible effects of roughness induced by the porous material (Rasheed 2001; Lukashevich et al. 2016b), location/extent of the porous material (Lukashevich et al. 2016a), and Darcy-flow effects within the porous material volume itself.

## 6.2 Frequency content

6.2.1 Experiments

The most amplified second-mode frequencies from Fig. 10, and the spectra for test conditions 2, 4, 6, 8, 10, and 12 in Table 1, were extracted and are provided by the black dots in Fig. 11a. Data from the porous material are not shown since their spectra never indicated such peaks. Impermeable data for turbulent spectra are also omitted. Many of the spectra in Fig. 10 indicate relatively broad second-mode peaks; therefore, after manually processing these data, a maximum uncertainty of ± 4 kHz of the extracted frequency was determined. Repeatability tests at the same freestream conditions indicated the most amplified second-mode frequencies to be the same from test to test within ± 2 kHz. This level of uncertainty is contained within the size of the black markers provided in Fig. 11a. The most amplified second-mode frequency data are non-dimensionalized via,

$$F = \frac{2\pi f}{u_\infty Re_\infty}, \tag{13}$$

as illustrated in Stetson et al. (1983), Marineau et al. (2017), and Kennedy et al. (2022). Following the scaling law shown in these references, these non-dimensional frequencies are then plotted against the stability Reynolds number, $R = \sqrt{Re_x}$. Note, this scaling law is similar to the one used on a flat plate in the work of Kegerise and Rufer (2016), both of which show good collapse of the current data set. The exponential line of best fit in Fig. 11a is given by $F = \left(3.3 \cdot 10^{-7}\right) \cdot \left(e^{\left(-8.4 \cdot 10^{-4}\right)R}\right)$ with a coefficient of determination value of $R^2 = 0.96$. These data show good agreement with previous planar and axisymmetric works (Stetson
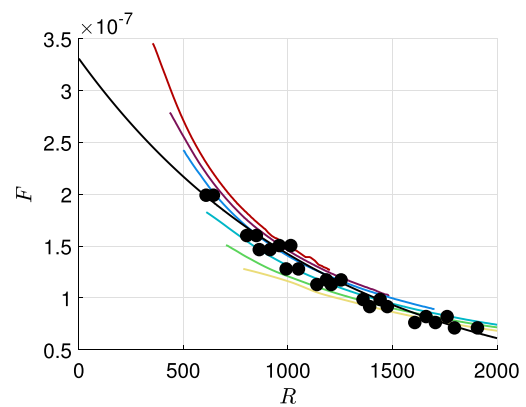
(a) Non-dimensionalized most amplified second-mode frequency, F, for the impermeable wall versus the stability Reynolds number, R. Black dots and line represent experimental data and a fit of experimental data, respectively. Colored lines represent computational data (see Table 4).
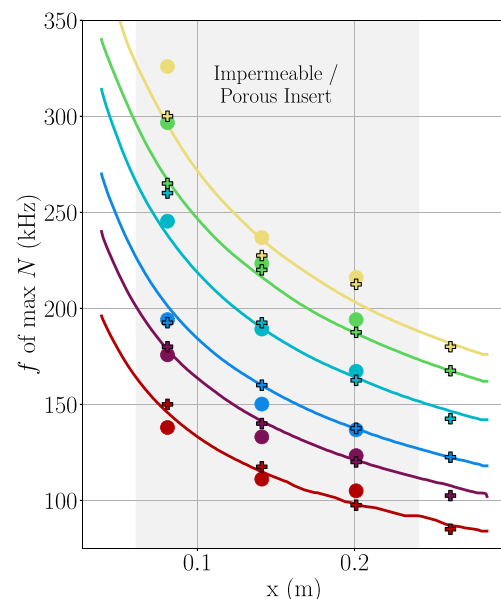
(b) Frequency of maximum N-factor for the impermeable wall versus x. Colored dots represent experimental data. Colored lines represent computational LST data. Colored plus signs represent transient CFD calculations pulsed with wall suction and blowing. See Table 4 for color information.

Fig. 11 Experimental and computational calculations of the most amplified second-mode frequency for the impermeable wall. Experimental uncertainty is contained within marker size

et al. 1983, 1991; Heitmann et al. 2011; Kegerise and Rufer 2016; Marineau et al. 2017; Kennedy et al. 2022).

6.2.2 Computations

Using the frequency-by-frequency spatial growth rates computed from LST, the N factors, N, for each frequency can be computed using the method discussed by Ingen (1956)

and shown in Eq. 14. The spatial growth rates are integrated cumulatively from x_0 to x^* showing how much a perturbation at a specific frequency would grow with no other input disturbances. In this formulation, x_0 is defined where the predicted growth rate crosses the neutral stability line and x^* is each location along the plate to where the cumulative integral is taken.

$$N(x^*) = \int_{x_0}^{x^*} \kappa_r(x)dx \qquad (14)$$

The most amplified second-mode frequencies at each location along the computational domain were extracted by determining which frequency has the largest N at each x location. This envelope is plotted in Fig. 11b with a single colored solid line for each of the six computational conditions with the impermeable wall (Table 4). Two methods of validation are employed to verify that the baseflow is correct and viable for use in LST. The first is the direct comparison to the experimentally observed second-mode frequencies. The colored dots in Fig. 11b represent the most amplified second-mode frequencies extracted from the corresponding experimental PCB spectra from Fig. 10 at each specific Reynolds number. The second form of validation depicted in Fig. 11b comes from the second-mode frequencies obtained from time-resolved CFD simulations triggered by a single pulse of wall suction and blowing (colored plus signs), described in Sec. 5.1. Similar to the experiments, the pressure at the wall was measured via time probes at each of the PCB locations and an FFT was employed to determine the peak second-mode frequencies.

Good agreement is observed for each of the six conditions, with the worst being between the LST and CFD at the first PCB location, where the introduced pulse simply has not had sufficient time to properly develop convectively into second-mode waves. Excellent agreement between LST and CFD is observed at the most downstream location, as expected. The impermeable-wall LST results are also overlaid on the scaled experimental data in Fig. 11a, where good agreement is once again observed. Computational porous results are not shown here. Due to the high absorption coefficient of the SiC foam, no clear traces of the second-mode instability in the LST was visible when incorporating the impedance boundary condition. This result further supports the observations of strong dampening in the raw experimental spectra (Fig. 10).

6.3 Growth rate

6.3.1 Experiments

Relative growth rates of the instability are generally described via N factor, N; however, N could not be calculated

(a) Relative growth

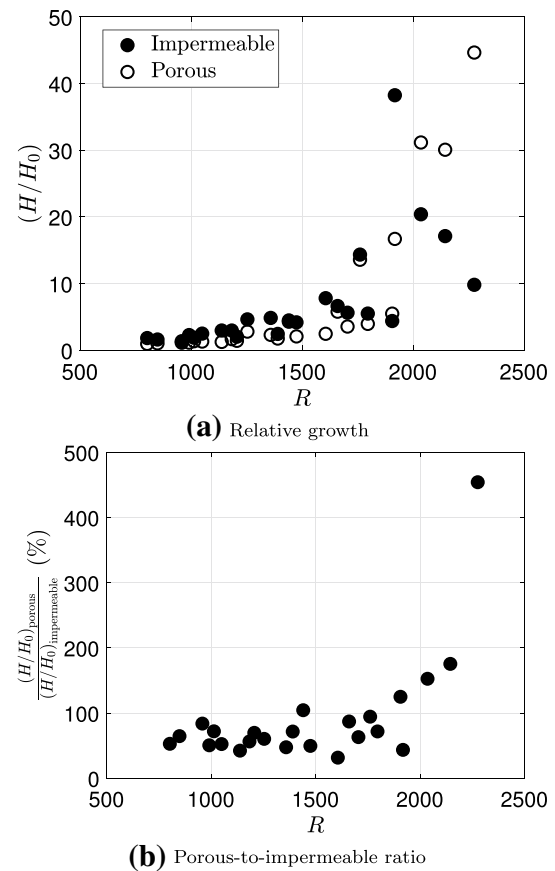**(b)** Porous-to-impermeable ratio

Fig. 12 Band-limited ($11 \leq f \leq 400$ kHz) relative amplitude growth behavior for impermeable (filled-in circle) and porous (open circle) materials

for the experimental porous data since they did not indicate instability-specific growth. Instead, the experimental growth comparisons between the impermeable and the porous data were conducted via band-limited relative amplitude integration. For each of the twelve wind-tunnel conditions, the spectral amplitude, G, of each sensor was integrated over a frequency band of $11 \leq f \leq 400$ kHz, and is given by the variable H. The band-limited integrated amplitude of sensor 1 for each test condition was considered G_0 since it provides the first measure of the potential instability, and is given by the variable H_0. The associated values for sensors 2 and 3 were then divided by this sensor-1 value, resulting in a measure of the relative amplitude growth for frequencies in the range of the expected instability mechanisms over the flat plate, H/H_0.

This relative growth was calculated for both the impermeable and porous data since it did not require growth at a particular frequency to be present. Figure 12a shows the relative growth results for the impermeable (filled-in black circles) and porous (open circles) data for each test condition. Figure 12b plots the relative growth of the porous data over the impermeable data as a percentage (i.e., values below 100%
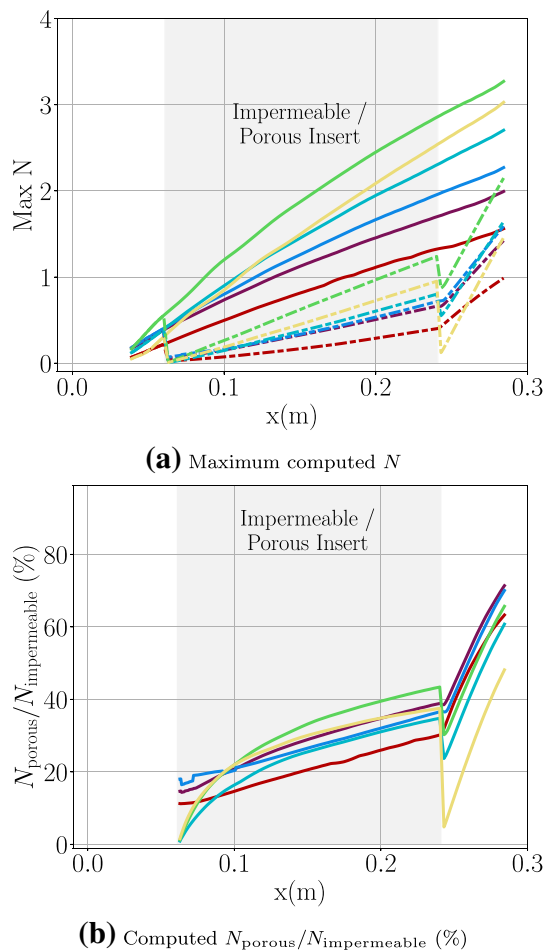
(a) Maximum computed N

(b) Computed $N_{porous}/N_{impermeable}$ (%)

Fig. 13 Maximum second-mode computed N along the test article integrated from LST results for the impermeable (solid line) and porous (dashed line) walls. See Table 4 for color information

indicate a porous-wall decrease in band-limited amplitude and values above 100% indicate a porous-wall increase in band-limited amplitude).

Similar to the spectral comparisons made in regards to Fig. 10, Fig. 12 illustrates that the porous material decreases band-limited amplitude ($11 \leq f \leq 400$ kHz) at lower R, but indicates similar overall relative amplitude growth to the impermeable material at higher R (i.e., transition to turbulence), which could be attributed to roughness effects. The porous-wall decrease in relative amplitude growth at lower R is mostly attributed to the clear absorption of the second-mode amplitude peaks observed in Fig. 10.

6.3.2 Computations

The LST was not limited in the same way as the experiments allowing for true N to be computed for the impermeable and porous walls. The envelope of the magnitude of the N curves are plotted in Fig. 13a. These curves are generated in

a similar way to the f of max N curves in Fig. 11b; however, rather than plotting the frequency where the N are at their greatest for each x location, the magnitude of N itself is plotted. Similar to Fig. 12b, the ratio $N_{porous}/N_{impermeable}$ of these computed results is shown as a percentage in Fig. 13b.

Figure 13 indicates that the magnitude of the N envelope increases with freestream Reynolds number from the lowest Reynolds number up until the second highest Reynolds number (green line). After that, the max N curve of the highest Reynolds number (yellow line) is decreased in magnitude in comparison to the second highest Reynolds number. This is an unexpected result, as LST using Blasius' solution as a base flow predicts that the spatial N value should continue to increase as freestream Reynolds number increases. It was verified that this is not due to under-resolution of the base flow or the grid on which LST was conducted. The unsteady pulsed wall CFD simulations yield similar results. In these results (not shown), the amplitude of the PSD measured from the pressure fluctuations at the wall also did not show the expected increase in amplitude from the second highest Reynolds number to the highest Reynolds number. Further investigation into this (most likely entailing more complex receptivity dynamics) is beyond the scope of this work.

In spite of this effect, all of the LST cases conducted with impedance boundary conditions (IBC) show an immediate decrease in the N at the beginning of the insert (i.e., the beginning of the gray shading in Fig. 13), and throughout the entire length of the insert, consistent with the experiments. Figure 13b shows $N_{porous}/N_{impermeable}$ to be between $10 - 40$ % over the porous insert, depending on the Reynolds number. Data in Fig. 13b for the three highest Reynolds numbers (Table 4, conditions 4, 5, and 6) indicate a steeper increase in $N_{porous}/N_{impermeable}$ at the beginning of the porous insert. It should be noted that the predicted impermeable-wall second-mode frequencies in this region are within the range where the JCA model requires extrapolation in frequency ($f > 300$ kHz) and should therefore be treated as less reliable. The three lower Reynolds numbers (Table 4, conditions 1, 2, and 3) therefore do not show this effect.

After the end of the porous insert and the reestablishment of the impermeable-wall boundary condition (i.e. infinite impedance), Figs. 13a and b show a significant increase in second-mode growth rate and N value. This is due to the reemergence of lower-frequency modes that would have otherwise been hidden underneath the envelope of the more dominant higher-frequency modes in the N envelope had the impedance boundary condition not been applied. This result is potentially indicative that a porous insert with limited extent may accentuate second-mode growth downstream of it, consistent with findings by Miller et al. (2022) on a sharp cone.

These results highlight the highly absorptive behavior of the SiC foam, and its general ability to dampen the

second-mode boundary-layer instability over a flat plate. They are also in good agreement with the bench-test and experimental findings throughout this study.

7 Conclusions

Unsteady surface pressure measurements have been carried out on a flat-plate test article in the Air Force Research Laboratory's Mach-6 Ludwieg Tube at a negative angle of attack using PCB pressure sensors. One impermeable (PEEK) and one porous (SiC foam) material were investigated. These experiments were supported by absorption bench tests and LST. The wind-tunnel $\frac{p'}{p_\infty}$ spectra for the impermeable wall were indicative of traditional second-mode instability behavior, with amplified second-mode peaks observed for $100 < f < 350$ kHz at lower unit Reynolds numbers and breakdown to turbulence for higher unit Reynolds numbers. The most amplified second-mode peaks were not observed in any of the porous-wall spectra; however, the spectra did indicate similar breakdown-to-turbulence behavior. The supporting bench tests measured high levels of acoustic absorption ($\beta > 0.90$) for the SiC foam, further supporting the experimental spectral behavior. An acoustic-absorption model was built from these bench tests and used as an impedance boundary condition in the supporting computations.

The most amplified experimental second-mode frequencies for the impermeable wall scale well with the F versus R scaling law utilized in earlier works. The LST computed frequencies of maximum N also showed good agreement with the experimental data.

The experimental relative amplitude growth were calculated via band-limited amplitude integration for $11 \leq f \leq 400$ kHz since the porous spectra were not indicative of the second-mode instability. Due to the porous walls ability to completely remove the characteristic second-mode spectral peaks, it was found that the relative growth in amplitude was less than for the impermeable wall until $R \approx 2000$, where the breakdown to turbulence behaved similarly to the impermeable-wall spectra. Computed N indicated analogous behavior — relative growth rates were significantly reduced ($N_{\text{porous}}/N_{\text{impermeable}} \approx 30\,\%$) over the axial span of the insert when the porous wall was present, after which, $N_{\text{porous}}/N_{\text{impermeable}}$ approached 100 %.

This study indicates that SiC foam has a strong ability to absorb acoustic waves characteristic of the hypersonic second-mode boundary-layer instability mechanism. This was indicated by experimental wind-tunnel results on a flat-plate test article, and supported by acoustic-absorption bench tests and LST computations. It is suggested that future works studying this technology investigate the surface-roughness effects of such a porous material, and the associated global transition-front phenomenon.

Author Contributions CLR, BLB, JJR, and KJ wrote the majority of the manuscript text. CLR and BLB conducted the wind-tunnel experiments and subsequent data processing with the assistance of JLH and MPB. KJ conducted the bench-test experiments and subsequent data processing with the assistance of CS. JJR conducted the computations and subsequent data processing with the assistance of CS. All authors reviewed the manuscript.

Data availability Interested parties may contact the corresponding author with inquiries.

Declarations

Conflict of interest The authors declare no competing interests.

References

Allard JF, Champoux Y (1992) New empirical equations for sound propagation in rigid frame fibrous materials. J Acoust Soc 91(6):3346–3353

Anderson J (2006) Hypersonic and high temperature gas dynamics, 2nd edn, American institute of aeronautics and astronautics, Inc., Reston, Virginia, chap 7

Bemis BL, Brun JL, Wanstall CT, Hill JL, Borg MP, Redmond JJ, Jantze MRK, Scalo C, Running CL (2023) Ultrasonically absorptive silicon-carbide foam for boundary-layer control. AIAA Paper 2023–0096

Champoux Y, Allard JF (1991) Dynamic tortuosity and bulk modulus in air-saturated porous media. J Appl Phys 70(4):1975–1979

Demetriades A (1974) Hypersonic viscous flow over a slender cone, part III: laminar instability and transition. AIAA Paper 1974–535

Egorov IV, Fedorov AV, Soudakov VG (2008) Receptivity of a hypersonic boundary layer over a flat plate with a porous coating. J Fluid Mech 601:165–187

Fedorov AV (2003) Receptivity of a high-speed boundary layer to acoustic disturbances. J Fluid Mech 491:101–129

Fedorov AV, Malmuth ND, Rasheed A, Hornung HG (2001) Stabilization of hypersonic boundary layers by porous coatings. AIAA J 39(4):605–610

Fedorov AV, Shiplyuk A, Maslov A, Burov E, Malmuth N (2003) Stabilization of a hypersonic boundary layer using an ultrasonically absorptive coating. J Fluid Mech 479:99–124

Fedorov A, Kozlov V, Shiplyuk A, Maslov A, Malmuth N (2006) Stability of hypersonic boundary layer on porous wall with regular microstructure. AIAA J 44(8):1866–1871

Force N (1992) Report of the defense science board task force on the national aerospace plane (NASP). Technical report, Defense

science board, office of the secretary of defense, Washington, DC 20301-3140

Fung KY, Ju H (2004) Time-domain impedance boundary conditions for computational acoustics and aeroacoustics. Int J Comput Fluid Dyn 18(6):503–511

Haga T, Kawai S (2019) On a robust and accurate localized artificial diffusivity scheme for the high-order flux-reconstruction method. J Comput Phys 376:534–563

Heitmann D, Kahler C, Radespiel R, Roediger T, Knauss H, Wagner S (2011) Non-intrusive generation of instability waves in a planar hypersonic boundary layer. Exp Fluids 50(2):457–464

Hsu PS, Jiang N, Jewell JS, Felver JJ, Borg MP, Kimmel RL, Roy S (2020) 100 kHz PLEET velocimetry in a Mach-6 Ludwieg tube. Opt Express 28(15):21982–21992

Ingen J (1956) A suggested semi-emperical method for the calculation of the boundary layer transition region. Technical Report V.T.H.-74, Technische Universiteit Delft, Delft, Netherlands

Johnson H, Gronvall J, Candler G (2009) Reacting hypersonic boundary layer stability with blowing and suction. AIAA Paper 2009-938

Kegerise MA, Rufer SJ (2016) Unsteady heat-flux measurements of second-mode instability waves in a hypersonic flat-plate boundary layer. Exp Fluids 57(130):1–15

Kendall JM (1975) Wind tunnel experiments relating to supersonic and hypersonic boundary-layer transition. AIAA J 13(3):290–299

Kennedy RE, Jewell JS, Paredes P, Laurence SJ (2022) Characterization of instability mechanisms on sharp and blunt slender cones at Mach 6. J Fluid Mech 936(39):1–24

Kimmel R (2003) Aspects of hypersonic boundary layer transition control. AIAA Paper 2003-772

Kimmel RL, Borg MP, Jewell JS, Lam K, Bowersox R, Srinivasan R, Fuchs S, Mooney T (2017) AFRL Ludwieg tube initial performance. AIAA Paper 2017-0102

Kopriva DA, Kolias JH (1996) A conservative staggered-grid Chebyshev multidomain method for compressible flows. J Comput Phys 125(1):244–261

Lukashevich S, Morozov S, Shiplyuk A (2016a) Experimental study of the effect of a passive porous coating on disturbances in a hypersonic boundary layer 2. Effect of the porous coating location. J Appl Mech Tech Phys 57(5):873–878

Lukashevich SV, Morozov SO, Shiplyuk AN (2016b) Combined influence of coating permeability and roughness on supersonic boundary layer stability and transition. J Fluid Mech 798:751–773

Lukashevich SV, Morozov SO, Shiplyuk AN (2018) Passive porous coating effect on a hypersonic boundary layer on a sharp cone at small angle of attack. Exp Fluids 59(130):1–11

Mack LM (1984) Boundary-layer linear stability theory. Tech. rep, DTIC Document

Malmuth N, Fedorov A, Shalaev V, Cole J, Hites M, Williams D, Khokhlov A (1998) Problems in high speed flow prediction relevant to control. AIAA Paper 1998-2695

Marineau EC, Moraru CG, Daniel DT (2017) Sharp cone boundary-layer transition and stability at Mach 14. AIAA Paper 2017-0766

Maslov AA, Shiplyuk AN, Sidorenko AA, Arnal D (2001) Leading-edge receptivity of a hypersonic boundary layer on a flat plate. J Fluid Mech 426:73–94

Miller SA, Redmond JJ, Jantze K, Scalo C, Jewell JS (2022) Investigation of second-mode instability attenuation over porous materials in Mach-6 quiet flow. AIAA Paper 2022-3530

Oddo R, Hill JL, Reeder MF, Chin D, Embrador J, Komives J, Tufts M, Borg M, Jewell JS (2021) Effect of surface cooling on second-mode dominated hypersonic boundary layer transition. Exp Fluids 62(144):1–18

Ort DJ, Dosch JJ (2019) Influence of mounting on the accuracy of piezoelectric pressure measurements for hypersonic boundary layer transition. AIAA Paper 2010-2292

Premasuthan S, Liang C, Jameson A (2014) Computation of flows with shocks using the spectral difference method with artificial viscosity, I: basic formulation and application. Comput Fluids 98:111–121

Rasheed A (2001) Passive hypervelocity boundary layer control using an ultrasonically absorptive surface. PhD thesis, California Institute of Technology, Pasadena, CA

Rasheed A, Hornung HG, Fedorov AV, Malmuth ND (2002) Experiments on passive hypervelocity boundary-layer control using an ultrasonically absorptive surface. AIAA J 40(3):481–489

Reed HL, Kimmel R, Schneider S, Arnal D, Saric W (1997) Drag prediction and transition in hypersonic flow. In: AGARD Conference Proceedings, AGARD 3:C15–C15

Roediger T, Knauss H, Kraemer E, Heitmann D, Radespiel R, Smorodsky BV, Bountin DA, Maslov AA (2008) Hypersonic instability waves measured on a flat plate at Mach 6. In: International conference on methods of aerphysical research (ICMAR)

Rosin GS (1972) Measurement of dynamic properties of acoustic materials

Saikia B, Brehm C (2022) Effect of distributed surface roughness on the stability of high-speed flows. AIAA Paper 2022-1212

Scalo C, Bodart J, Lele SK (2015) Compressible turbulent channel flow with impedance boundary conditions. Phys Fluids 27(3):035107

Sivasubramanian J, Fasel HF (2014) Numerical investigation of the development of three-dimensional wavepackets in a sharp cone boundary layer at Mach 6. J Fluid Mech 756:600–649

Sousa VCB (2022) A novel subfilter closure for compressible flows and its application to hypersonic boundary layer transition. PhD thesis, Purdue University

Sousa VCB, Patel D, Chapelier JB, Wartemann V, Wagner A, Scalo C (2019) Numerical investigation of second-mode attenuation over carbon/carbon porous surfaces. J Spacecr Rockets 56(2):319–332

Stetson KF (1983) Nosetip bluntness effects on cone frustum boundary layer transition in hypersonic flow. AIAA Paper 1983-1763

Stetson KF, Kimmel RL, Thompson ER, Donaldson JC, Siler LG (1991) A comparison of planar and conical boundary layer stability and transition at a Mach number of 8. AIAA Paper 1991-1639

Stetson K, Kimmel R (1993) On the breakdown of a hypersonic laminar boundary layer. AIAA Paper 1993-0896

Stetson K, Thompson E, Donaldson J, Siler L (1983) Laminar boundary layer stability experiments on a cone at Mach 8. I-Sharp cone. AIAA Paper 1983-1761

Sutherland W (1893) The viscosity of gases and molecular force. Lond, Edinb, Dublin Philos Mag J Sci 36(223):507–531

Tsyryulnikov LS, Mironov SG (2004) Determination of ultrasound absorption characteristics of thin porous coatings. Thermophys Aeromech 11(4):509–518

van Driest ER, Boison JC (1957) Experiments on boundary-layer transition at supersonic speeds. J Aeronaut Sci 24(12):885–899

Wagner A, Kuhn M, Schramm JM, Hannemann K (2013) Experiments on passive hypersonic boundary layer control using ultrasonically absorptive carbon-carbon material with random microstructure. Exp Fluids 54(10):1606

Wagner A, Hannemann K, Kuhn M (2014) Ultrasonic absorption characteristics of porous carbon-carbon ceramics with random microstructure for passive hypersonic boundary layer transition control. Exp Fluids 55(6):1750

Wartemann V, Wagner A, Kuhn M, Eggers T, Hannemann K (2015) Passive hypersonic boundary layer transition control using an ultrasonically absorptive coating with random microstructure: computational analysis based on the ultrasonic absorption properties of carbon–carbon. Procedia IUTAM 14:413–422

Welch PD (1967) The use of fast fourier transform for the estimation of power spectra: a method based on time averaging over short, modified periodograms. IEEE Trans Audio Electroacoust 15(2):70–73

Wendt V, Kreplin HP, Höhler G, Grosche FR, Krogmann P, Simen M (1993) Planar and conical boundary layer stability experiments at Mach 5. AIAA Paper 1993-5112

Yates HB, Matlis EH, Juliano TJ, Tufts MW (2020) Plasma-actuated flow control of hypersonic crossflow-induced boundary-layer transition. AIAA J 58(5):1–16